

LA-UR-15-21360

Approved for public release; distribution is unlimited.

Title: Load transfer and relaxation in a NiAl-strengthened ferritic alloy
studied by in-situ neutron diffraction

Author(s): Sun, Zhiqian
Sisneros, Thomas A.
Clausen, Bjorn
Song, Gian
Gao, Yanfei
Liaw, Peter

Intended for: Nature Materials

Issued: 2015-02-24

Disclaimer:

Los Alamos National Laboratory, an affirmative action/equal opportunity employer, is operated by the Los Alamos National Security, LLC for the National Nuclear Security Administration of the U.S. Department of Energy under contract DE-AC52-06NA25396. By approving this article, the publisher recognizes that the U.S. Government retains nonexclusive, royalty-free license to publish or reproduce the published form of this contribution, or to allow others to do so, for U.S. Government purposes. Los Alamos National Laboratory requests that the publisher identify this article as work performed under the auspices of the U.S. Department of Energy. Los Alamos National Laboratory strongly supports academic freedom and a researcher's right to publish; as an institution, however, the Laboratory does not endorse the viewpoint of a publication or guarantee its technical correctness.

Load transfer and relaxation in a NiAl-strengthened ferritic alloy studied by in-situ neutron diffraction

Z. Sun¹, T. Sisneros², G. Song¹, B. Clausen², Y. Gao¹ & P. K. Liaw¹

1. Department of Materials Science and Engineering, The University of Tennessee, Knoxville, Tennessee 37996, USA

2. Los Alamos National Laboratory, Los Alamos, New Mexico 87545, USA

In-situ tensile tests under neutron diffraction at 364 and 506 °C were performed on a NiAl-strengthened ferritic alloy to explore the load partitioning between the matrix and precipitates during deformation. The deformed microstructure was characterized by the transmission electron microscope. At 364 °C, load transfers to precipitates from the matrix anisotropically on the grain scale. The lattice strain of <100>-oriented precipitates relative to the loading direction is approximately four times as much as that in <111>-oriented ones. The experimental results are compared with the Eshelby model and crystal-plasticity finite element analysis. Excellent agreement between the experimental result and finite element modeling has been found at 364 °C. However, load relaxation around NiAl-type precipitates occurs at 506 °C, which is probably due to the local thermally-activated dislocation rearrangement. Effects of the load partitioning among constituent phases on the high-temperature creep deformation have been discussed.

Most engineering materials contain multiple phases. Generally, the strengthening effects in materials containing reinforced phases originate from two aspects: (1) impeding the dislocation movement by the interaction with reinforcements through mechanisms, e.g., the dislocation cutting, Orowan bowing, and dislocation climb [1, 2]; (2) load-carrying capability of stiff reinforcements due to elastic and plastic misfit [3-6]. For metal-matrix composites (MMCs), the first strengthening effect is probably negligible due to the large inter-particle distance. The extent of the load partitioning is associated with factors, e.g., the reinforcement volume fraction, morphology, and orientation. If the thermally-activated movement gets involved, the load on reinforcements tends to relax [3, 7-9]. It is usually difficult to distinguish separated roles of each phase by only considering the macroscopic stress-strain data. By combining with modeling and electron microscope, diffraction method services as a powerful tool to reveal the load partitioning [6, 10-12] and deformation mechanisms [13-16] in engineering materials.

Coherent B2 NiAl-type precipitates (β) are employed to strengthen the α -iron matrix (α) for elevated-temperature applications in power plants [17-20]. The load transfer efficiency between α and β strongly affects the creep resistance of NiAl-strengthened ferritic alloys. The objective of this paper is to investigate the load transfer and relaxation between α and β during tensile tests through in-situ neutron diffraction. The experimental results have been compared with the Eshelby model and crystal-plasticity finite element (FE) analysis. The transmission electron microscope (TEM) has been employed to study the microstructures of virgin and deformed specimens. This study will provide new insights in developing multiphase alloys or composites.

Results

Typical β morphology is shown in Figure 1. Precipitates are spherical, suggesting small coherency strain between the matrix and precipitates. The average precipitate size is around 108 nm [21] with the volume fraction of $\sim 15 - 16\%$ [19]. β is not chemical stoichiometric and displays solubility of other elements. Teng et al. reported the β composition as $\text{Ni}_{41.2}\text{Al}_{43.6}\text{Fe}_{12.7}\text{Cr}_{0.8}\text{Mo}_{1.4}$ for the specimen aged for 100 h at 700 °C. Contrast is presented within each precipitate, which is probably due to the nano-sized iron-rich disordered phase forming during the cooling process [19]. Similar phenomenon is also reported by Vo et

al [20]. The superlattice reflections from ordered B2 precipitates (e.g., 100, 111, and 210) are observed, besides the well-overlapped fundamental peaks, which are common for α and β (see Supplementary Figure S1). The lattice mismatch between α and β is determined to be $\sim 0.1\% - 0.14\%$ at 364 and 506 °C. The nominal tensile stress-strain curves at 364 and 506 °C are plotted in Figure 2. Total 14 steps (the load control: 10, 100, 200, 300, 400, 500 and 600 MPa; the strain control: 0.81%, 0.91%, 1.02%, 1.23%, 1.43%, 1.64%, and 1.85%) were used at 364 °C, while 13 steps at 506 °C (the load control: 10, 100, 150, 200, 250, 300 and 350 MPa; 0.29%, 0.50%, 1.02%, 1.80%, 2.84%, and 3.88%). The specimen yielded at the stress between 500 to 600 MPa at 364 °C, and 450 to 500 MPa at 506 °C. In the plastic regime, the applied load decreases during the 30-min neutron counting period with a fixed crosshead. The decay is more pronounced at 506 °C. The stress-time curves of the first stress decay for both tests are included in Figure 2. The stress drops rapidly from 643 to 627 MPa at 364 °C and from 467 to 458 MPa at 506 °C in 24 seconds. The stress decay rate gradually slows down in both cases, and the applied stress approaches 605 MPa at 364 °C and 430 MPa at 506 °C at the end. The average stress (shown as red spots in Figure 2) at 364 °C linearly goes up from 611 to 725 MPa as the strain increases from 0.81% to 1.85%, while the average stress at 506 °C saturates around ~ 531 MPa. The diffraction pattern evolves as the test going. Since both phases have similar elastic stiffness [17, 22], the fundamental reflections remain overlapped in the elastic regime. However, they gradually separate upon plastically loading, indicating load transfer to β from α . The extent of the peak separation strongly depends on the orientation. An example of the peak separation is given in the inset of Figure 2(a). The overlapped (200) peak position before loading is 1.4472 Å, while it becomes separated and the peak positions are 1.4560 (α) and 1.4728 Å (β) at the strain of $\sim 1.85\%$.

The evolutions of lattice strains (i.e., $\varepsilon_{P,100}$, $\varepsilon_{P,111}$, $\varepsilon_{P,210}$, and ε_M) at 364 °C are shown in Figures 3 as functions of the initial applied stress and macrostrain. ε_M responses linearly with the applied stress till 500 MPa as expected by materials obeying Hooke's law. The elastic modulus is determined to be ~ 158 GPa by fitting the stress vs. lattice strain. Afterwards ($\sigma > 500$ MPa or $\varepsilon > 0.34\%$), ε_M remains essentially

constant at $\sim 0.38\%$. The $\varepsilon_{P,hkl}$ evolution strongly depends on their crystalline orientations relative to the loading direction in both elastic and plastic regimes. The diffraction elastic moduli of β in $\langle 100 \rangle$, $\langle 111 \rangle$, and $\langle 210 \rangle$ directions are estimated to be 109, 228, and 154 GPa, respectively. The load transfers to precipitates upon the plastic deformation. $\varepsilon_{P,100}$ and $\varepsilon_{P,210}$ continue to increase in the plastic regime. It seems that the linear relationship between the lattice strain and macrostrain holds [Figure 5(b)]. The slopes are ~ 0.69 and 0.44 for $\varepsilon_{P,100}$ and $\varepsilon_{P,210}$, respectively. On the contrary, $\varepsilon_{P,111}$ increases much slower if any and remains $\sim 0.42\%$. Finally, $\varepsilon_{P,100}$ reaches as high as 1.62% at the macrostrain of 1.86% , which is approximate four times as much as $\varepsilon_{P,111}$. The FE modeling results are in excellent agreement with the experimental data. It confirms that precipitates deform elastically in this case. The stress on precipitates in the loading direction reaches ~ 1.25 GPa at the end of the test based on the model.

The evolutions of $\varepsilon_{P,100}$, $\varepsilon_{P,111}$, $\varepsilon_{P,210}$, and ε_M at 506°C are shown in Figures 4 as a function of the macrostrain. The behavior in the elastic regime follows the same trend as that at 364°C . In the plastic regime, ε_M almost stays constant at $\sim 0.35\%$, and even slightly decreases as the macrostrain increases. $\varepsilon_{P,100}$ and $\varepsilon_{P,210}$ increase at the beginning, and gradually saturate at 1.3% for $\varepsilon_{P,100}$ and 0.84% for $\varepsilon_{P,210}$. At the same time, $\varepsilon_{P,111}$ remains at $\sim 0.29\%$ in the plastic regime. The FE predicted results are symmetrically larger than experimental values in the plastic region, which results from the load relaxation around precipitates as discussed later. Note that we do not consider such relaxation in the FE model.

The representative micrographs of deformed specimens are shown in Figure 5. β shows strong interaction with dislocations. A large number of entangled dislocation and loops are observed around precipitates. Orowan bypass is likely to dominate the deformation. Large strain field is presented near precipitates [Figure 5(b)]. Mechanically, dislocation loops accommodate the plastic misfit between α and β , and lead to the internal stress observed by neutron diffraction (ND) in Figure 3. The magnitude of the plastic misfit is related to the spatial arrangement of these dislocation loops. Because of the high local stress produced in precipitates and nearby matrix, arrays of dislocation loops are not stable. The load relaxation process can occur through the rearrangement of these dislocations.

Discussions

Based on the Eshelby model (see Supplementary), the mean stress on β in the loading direction, $\langle\sigma\rangle_{P,3}$, can be expressed as

$$\langle\sigma\rangle_{P,3} = E \frac{7-5\nu}{15(1-\nu^2)} \varepsilon^P \quad (1)$$

where E is the elastic modulus, ν is the Poisson's ratio, ε^P is the overall plastic strain, and subscript “3” means the loading direction. According to Eq. (1), $\langle\sigma\rangle_{P,3}$ is linearly proportional to ε^P . Taking E as 158 GPa and ν as 0.3, it is predicted that $\sigma_{P,3} \sim 64\varepsilon^P$ (GPa).

Based on the FE modeling, the stress on precipitates in the loading direction is plotted against the plastic strain in Figure 6(a). The stress quickly increases at the beginning, and then follows the linear relationship with the plastic strain. However, the slope is smaller than that predicted by Eq. (1), and varies as the function of the strain-hardening related parameter, h_0 (Table 1). Since the matrix is plastically deformed and precipitates are in the elastic region, precipitates would resist being forced by the matrix. Given other conditions, the matrix with more pronounced strain-hardening rate (large h_0) could force precipitates elastically deformed more efficiently (large plastic strain) as shown in Figure 6(a). We conclude that the load transfer efficiency is not as high as that predicted by the Eshelby model, and depends on the strain-hardening capability of the matrix.

Microscopically, the lattice strain evolution shows strong dependence on the crystalline orientation (Figure 3). In order to understand the underlying reasons for such anisotropic behavior, $\varepsilon_{P,hkl}$ due to the plastic deformation is plotted against the plastic strain of the matrix in $\langle 100 \rangle$ -, $\langle 111 \rangle$ -, and $\langle 210 \rangle$ -oriented grains in Figure 6(b). Two interesting points are worthy noticing. First, the plastic deformation is inhomogeneous among grains ($\langle 100 \rangle$: 2.4%; $\langle 111 \rangle$: 1.2%; and $\langle 210 \rangle$: 2.3%). Note that the macro plastic strain for the test at 364 °C is $\sim 1.4\%$. Second, the lattice strain increases rapidly at the beginning, and then follows the linear relationship against the corresponding plastic strain of the matrix. The slopes are ~ 0.40 , 0.20 and 0.28 for $\langle 100 \rangle$ -, $\langle 111 \rangle$ -, and $\langle 210 \rangle$ -oriented precipitates, respectively. $\varepsilon_{P,111}$, $\varepsilon_{P,210}$, and $\varepsilon_{P,100}$ becomes larger in order at the same matrix plastic strain. The fact can be explained by the

elastic anisotropic of precipitates. As stated above, $\langle 111 \rangle$ has the largest elastic diffraction constant, while $\langle 100 \rangle$ is the elastic soft direction. Precipitates in the stiff direction resist being pulled by the matrix. Both factors contribute to the anisotropic lattice strain evolution as shown in Figure 3. However, the stress on β (by roughly multiplying the lattice strain with the diffraction elastic constant) at the same matrix plastic strain in three orientation is quite close.

As shown in Figure 4, the FE predicted lattice strains are systematical larger than the experimental results in $\langle 100 \rangle$, $\langle 111 \rangle$, and $\langle 210 \rangle$ directions at 506 °C. Two origins are speculated: (1) the stress relaxation of β occurs through possible mechanisms, e.g., the interface sliding and diffusion, and local dislocation movement [3]; (2) β yields and loses the capability to carry further load. If the latter assumption holds, the strain hardening exponent in $\langle 100 \rangle$ -orientated precipitates would be ~ 0.5 . However, it is much higher than the value (~ 0.1) reported by Pascoe et al. [23]. This suggests that load relaxation of β occurs during the holding.

For the observed stress decay, the activation volume, v^* , can be described by [24]

$$v^* = \sqrt{3}kT \left(\frac{\partial \ln \dot{\sigma}}{\partial \sigma} \right). \quad (2)$$

where k is the Boltzmann constant, T is the temperature, $\dot{\sigma}$ is the stress decreasing rate, and σ is the applied stress. See supplementary for details. The activation volume provides important information regarding possible deformation mechanisms [24-27]. $\ln \dot{\sigma}$ is plotted against σ for the first stress decay of both tests in Figure 7. At 364 °C, the linear relationship between $\ln \dot{\sigma}$ and σ is well satisfied, and the activation volume is estimated to be $\sim 183 b^3$, where b is the Burgers vector ($b = 2.508$ and 2.514 \AA at 364 and 506 °C, respectively). The dislocation forest cutting might govern the deformation. The plastic strain induced by the dislocation movement offsets some elastic strain in α , and hence, part of the work hardening in α quickly disappeared. This is why ε_M remains constant after yielding as shown in Figure 3. However, two linear sections are observed in the $\ln \dot{\sigma}$ vs. σ plot at 506 °C [Figure 7(b)]. The activation volumes are estimated to be $\sim 298 b^3$ from 467 to 456 MPa and $\sim 109 b^3$ from 455 to 433 MPa, suggesting two distinct deformation mechanisms. Similarly, the dislocation forest cutting probably

dominates the initial stress decay from 467 to 456 MPa in the initial 45 seconds. Afterwards, dislocations around β possibly rearrange themselves with the activation volume of $109 b^3$ in order to reduce the plastic misfit between α and β . The thermally-activated dislocation rearrangement at 506 °C probably leads to the load relaxation observed in Figure 4.

Concerning the creep deformation of particle-strengthened alloys and MMCs under a constant external stress, one scenario is that the load keeps transferring to stiff reinforcements, and the creep strain rate eventually approaches to zero upon the matrix reaching a uniform hydrostatic state as the creep proceeds [28]. As a matter of fact, it does not hold since the stress relaxation processes operate at high homologous temperatures.

The load-carrying capability of β is probably limited during the creep deformation under expected service conditions in fossil-energy power plants. First of all, since the strain hardening of the matrix is small at high temperatures (≥ 650 °C), the load-transfer efficiency itself is low, as discussed above. Next, the load relaxation processes probably dominate the creep deformation. The rate of stress relaxation is governed by many factors, e.g., the inclusion size and morphology, strain rate, and temperature. Rösler et al. [7] and Koeller and Raj [29] investigated the relaxation process by diffusion around reinforcements. The mass transport from compressed sides to sides under tension is arisen due to the presence of the normal stress gradients along the interface between the matrix and precipitates. They concluded that the diffusional flow is slow for large inclusions with a high aspect ratio. Experimentally, Nieh et al. [30, 31] demonstrated that Al/20 vol.% SiC whisker is more creep resistance than Al/30 vol.% SiC particulate at 288 °C with the creep rate slower by one to two orders of magnitude. Tomota et al. [10] also reported that the plate-shaped cementite is more effective to carry load than the spherical particles in tensile tests of a hyper-eutectoid steel. In particular, the small lattice mismatch between α and β in FBB8 probably means weak interaction between dislocations and precipitates. Therefore, the stress relaxation around nano-sized spherical β could be severe. Huang et al. [17] performed in-situ creep study on FBB8 at 700 °C under neutron diffraction. They found that the lattice strains of both phases in the loading direction approximately keep constant in the range from 0.05% to 0.06%, and the magnitude of the lattice strain of

α is $\sim 0.01\%$ higher than that of β during the creep deformation at 107 MPa. It means that load does not continuously transfer toward precipitates in their study. The presence of reinforcements could not be helpful, and even detrimental to the creep resistance considering that reinforcements cannot carry the larger share of load under certain conditions [32]. In order to avoid the strength reduction by the stress relaxation, consideration concerning the reinforcement shape, size, and lattice mismatch between the matrix and reinforcements for specific loading conditions is necessary. It is interesting to note that Rösler and Bäker [33] proposed the idea of dual-scale particle strengthening for the design of high-temperature materials by the combination of the dispersion strengthening and load-transfer strengthening.

Methods

A NiAl-strengthened ferritic alloy, designated as FBB8 (Fe-6.5Al-10Ni-10Cr-3.4Mo-0.25Zr-0.005B, weight percent), was investigated in this study. Ingots ($\sim 12.7 \times 25.4 \times 1.9$ cm) were prepared by Sophisticated Alloys, Inc., using the vacuum induction melting. Hot isostatic pressing (1,200 °C/103 MPa/4 h) was performed to minimize casting porosity. Specimens encapsulated into evacuated quartz tube were solution treated at 1,200 °C for 1 hour followed by air cooling, and then, aged for 100 h at 700 °C. The average grain size is ~ 100 μm .

Two threaded tension specimens with the gauge length of 41.28 mm and the gauge diameter of 6.35 mm were in-situ loaded in the vacuum environment at the Spectrometer for the Materials Research at Temperature and stress (SMARTS) of the Los Alamos Neutron Science Center at the Los Alamos National Laboratory. A detailed description of its experimental setup can be found in Ref. [34]. The sample temperatures, measured by thermocouples attached to specimens, were 364 and 506 °C. The preload was ~ 10 MPa in both cases. The step-loading method was used, and time-of-flight ND patterns from crystalline planes normal (axial) and parallel (transverse) to the loading direction were acquired by two sets of detectors with the counting time of 30 minutes. The ND spectrum represents the average information in the counting period. Only diffraction spectra from crystalline planes normal to the loading direction were analyzed in this study. The macrostrain was monitored by the high-temperature extensometer.

The lattice constant, a , was obtained by the Rietveld refinement of the whole spectrum using GSAS [35], while the single-peak fitting procedures in GSAS was employed to determine the interplanar spacing (d_{hkl}). Two kinds of lattice strains were calculated based on the results: (1) the average phase lattice strain of the matrix, defined as $\varepsilon_M =$

$\frac{a-a_0}{a_0}$, where a_0 is the reference lattice constant of the matrix before loading; (2) the $\{hkl\}$ single-peak lattice strain of precipitates, defined as $\varepsilon_{P,hkl} = \frac{d_{hkl}-d_0}{d_0}$, where d_0 is the reference interplanar spacing of $\{hkl\}$ planes before loading. The subscript “M” stands for the matrix, and “P” for precipitates. In order to avoid artificial errors, we did not attempt to separate overlapped peaks considering the weak intensity of superlattice reflections from β . In this paper, the crystalline orientation is relative to the loading direction.

TEM images were taken using a Zeiss Libra 200 model. The specimens were prepared through electropolishing in a Fischione twin-jet polisher followed by the ion milling with the voltage of 3.5 keV for about ten minutes. The electrolyte of 5 vol.% HCl in ethanol was used at room temperature, and the current was controlled to be 6 – 8 μ A.

The crystal-plasticity FE analysis was performed, using the commercial software Abaqus 6.11. The Abaqus user-defined material (UMAT) subroutine by Huang [36] was used. Total 729 ($9 \times 9 \times 9$) randomly-oriented cubic grains are used in the model (see Supplementary Figure S1). Each grain consists of 64 elements and ten of them (eight in the center plus two outside) are set to be precipitates. Precipitates are set to only deform elastically. See Supplementary for more details.

Acknowledgment

The research is supported by the Department of Energy (DOE), Office of Fossil Energy Program, under Grants of DE_09NT0008089 and DE-FE0005868 with Mr. Richard Dunst, Mr. Vito Cedro, and Dr. Patricia Rawls as the program managers. The work has benefitted from the use of Lujan Neutron Scattering Center at LANSCE, which is funded by the Office of Basic Energy Science (DOE). Los Alamos National Laboratory is operated by the Los Alamos National Security LLC under the DOE Contract DE-AC52-06NA-25396.

References

1. E. Nembach, G. Neite, Progress in Materials Science 29 (1985) 177-319.
2. E. Nembach, Particle Strengthening of Metals and Alloys, John Wiley & Sons, Inc., New York, 1997.
3. T.W. Clyne, P.J. Withers, An Introduction to Metal Matrix Composites, Cambridge University Press, New York, 1993.
4. H. Lilholt, Materials Science and Engineering: A 135 (1991) 161-171.
5. M.R. Daymond, H.G. Priesmeyer, Acta Mater. 50 (2002) 1613-1626.
6. E.C. Oliver, M.R. Daymond, P.J. Withers, Acta Materialia 52 (2004) 1937-1951.
7. J. Rösler, G. Bao, A.G. Evans, Acta Metall. Mater. 39 (1991) 2733-2738.
8. J. Rösler, A.G. Evans, Mater. Sci. Eng. A 153 (1992) 438-443.
9. P. Sofronis, R.M. McMeeking, Mechanics of Materials 18 (1994) 55-68.
10. Y. Tomota, P. Lukas, D. Neov, S. Harjo, Y.R. Abe, Acta Mater. 51 (2003) 805-817.
11. A.J. Allen, M.A.M. Bourke, S. Dawes, M.T. Hutchings, P.J. Withers, Acta Metall. Mater. 1992 (1992) 2361-2373.
12. J. Coakley, D. Dye, Scripta Materialia 67 (2012) 435-438.
13. M.R. Daymond, M. Preuss, B. Clausen, Acta Materialia 55 (2007) 3089-3102.
14. E.M. Francis, B.M.B. Grant, J.Q.d. Fonseca, P.J. Phillips, M.J. Mills, M.R. Daymond, M. Preuss, Acta Materialia 74 (2014) 18-29.
15. S. Ma, V. Seetharaman, B.S. Majumdar, Acta Materialia 56 (2008) 4102-4113.
16. Y.-D. Wang, H. Tian, A.D. Stoica, X.-L. Wang, P.K. Liaw, J.W. Richardson, Nature Materials 2 (2003) 101-106.
17. S. Huang, D.W. Brown, B. Clausen, Z. Teng, Y. Gao, P.K. Liaw, Metallurgical and Materials Transactions A 43 (2011) 1497-1508.
18. C. Stallybrass, A. Schneider, G. Sauthoff, Intermetallics 13 (2005) 1263-1268.
19. Z.K. Teng, M.K. Miller, G. Ghosh, C.T. Liu, S. Huang, K.F. Russell, M.E. Fine, P.K. Liaw, Scripta Materialia 63 (2010) 61-64.
20. N.Q. Vo, C.H. Liebscher, M.J.S. Rawlings, M. Asta, D.C. Dunand, Acta Materialia 71 (2014) 89-99.
21. Z. Sun, G. Song, J. Ilavsky, G. Ghosh, P.K. Liaw, *Coarsening behavior of NiAl-type precipitates in a ferritic alloy, submitted to Acta Mater.* 2014.
22. D.B. Miracle, Acta Metall. Mater. 41 (1993) 649-684.
23. R.T. Pascoe, C.W.A. Newey, Metal Science 2 (1968) 138-143.
24. Q. Wei, J. Mater. Sci. 42 (2007) 1709-1727.
25. H. Conrad, S. Frederick, Acta Metall. 10 (1962) 1013-1020.
26. C.Y. Jeong, S.W. Nam, J. Ginsztler, Materials Science and Engineering A 264 (1999) 188-193.
27. Y.M. Wang, A.V. Hamza, E. Ma, Acta Mater 54 (2006) 2715-2726.
28. T. Mori, J.H. Huang, M. Taya, Acta Mater 45 (1997) 429-438.
29. R.C. Koeller, R. Raj, Acta Metall. 26 (1978) 1551-1558.
30. T.G. Nieh, Met. Trans. A 15 (1984) 139-146.
31. T.G. Nieh, K. Xia, T.G. Langdon, Journal of Engineering Materials and Technology 110 (1988) 77-82.
32. H.M.A. Winand, A.F. Whitehouse, P.J. Withers, Materials Science and Engineering A 284 (2000) 103-113.
33. J. Rösler, M. Bäker, Acta Mater 48 (2000) 3553-3567.
34. S. Ma, D. Brown, M.A.M. Bourke, M.R. Daymond, B.S. Majumdar, Materials Science and Engineering: A 399 (2005) 141-153.
35. A.C. Larson, R.B. Von Dreele, *General Structure analysis system (GSAS)*. 1994, Los Alamos National Laboratory Report LAUR. p. 86-748.

36. Y. Huang, *A user-material subroutine incorporating single crystal plasticity in the ABAQUS finite element program*, in *Mechanical Report 179*. 1991, Harvard University

Table 1. The slope (GPa) of the relationship between $\langle \sigma \rangle_{P,3}$ and ε^P .

Eshelby model	$h_0 = 500$	$h_0 = 300$	$h_0 = 100$
64	43	32	28

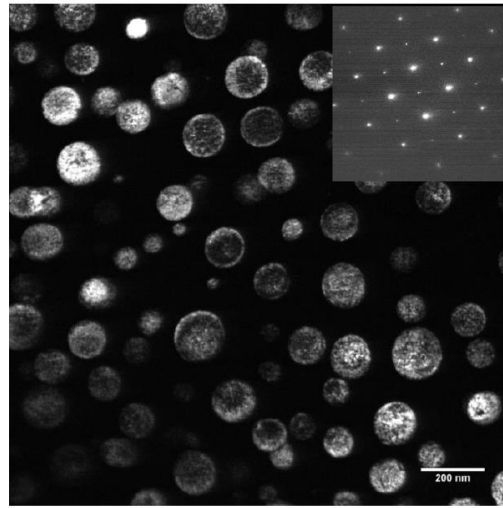
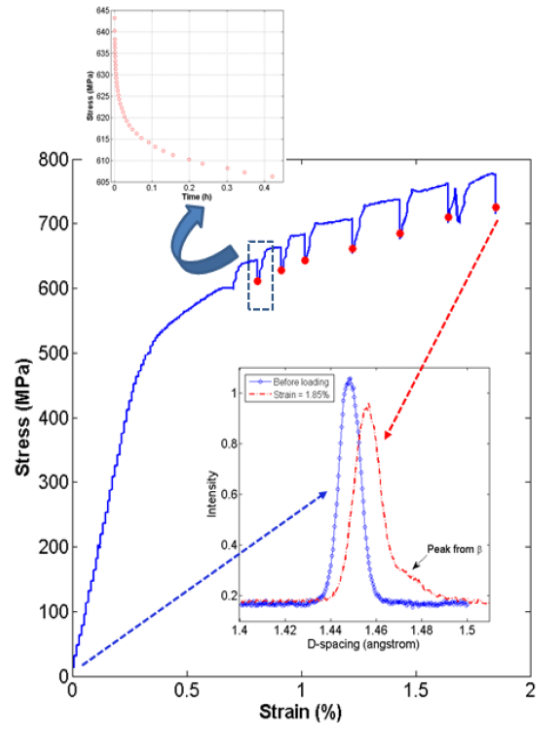
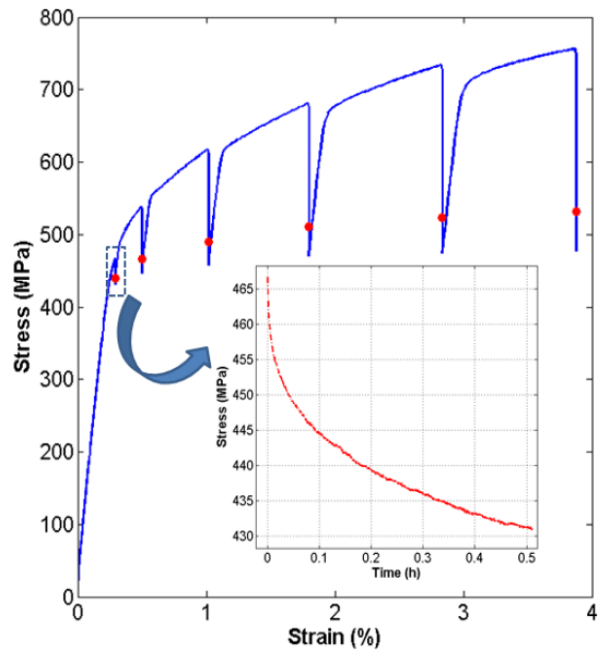


Figure 1. The dark-field (DF) images of β using 100 reflection with the inset showing the diffraction pattern.



(a)



(b)

Figure 2. The stress vs. strain curves of FBB8 at (a) 364 and (b) 506 °C, together with the first stress decay curves as a function of time. The average stress in each step is marked as red spots. The (200) peak separation is shown in the inset of (a).

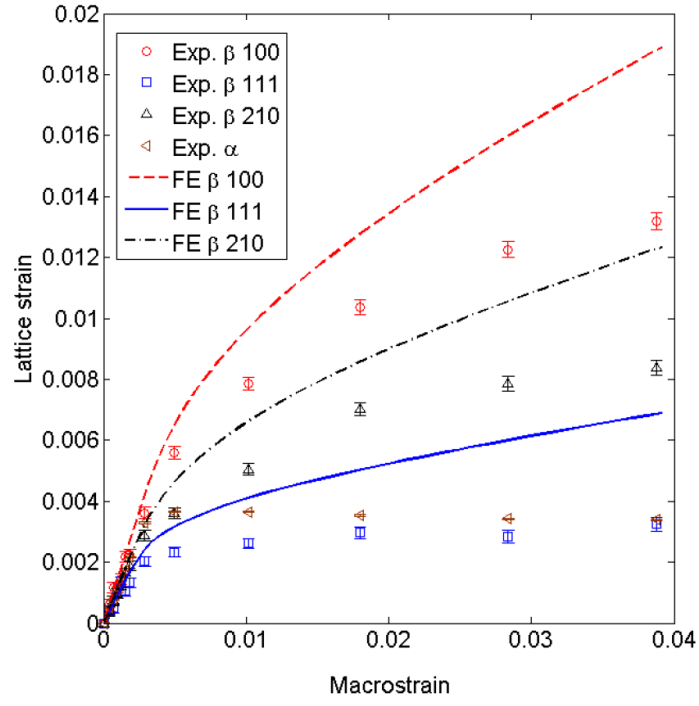
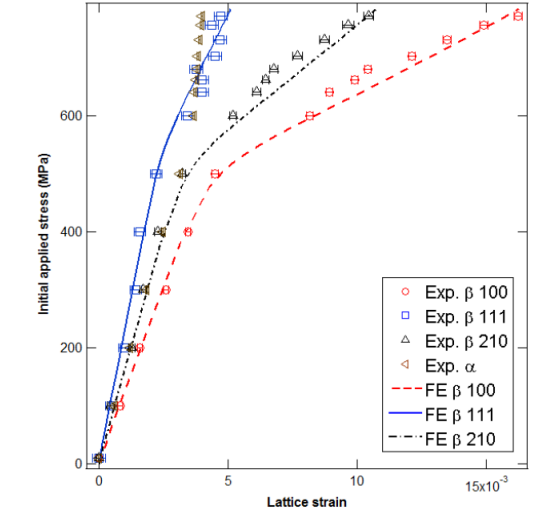
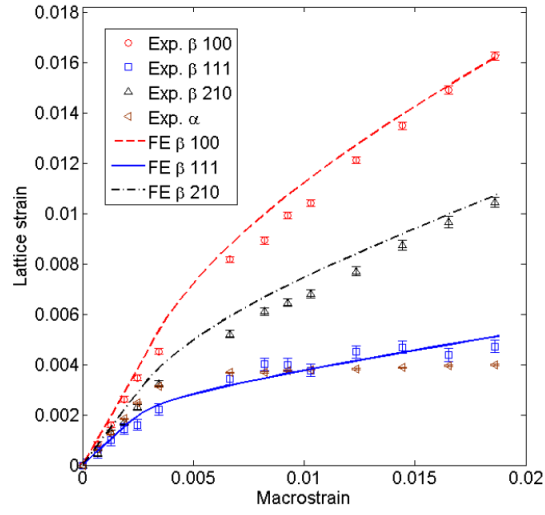


Figure 4. The evolutions of $\varepsilon_{p,100}$, $\varepsilon_{p,111}$, $\varepsilon_{p,210}$, and ε_M as the function of the macrostrain at 506 °C. The experimental data are denoted as points, while the FE analysis results are presented as lines.

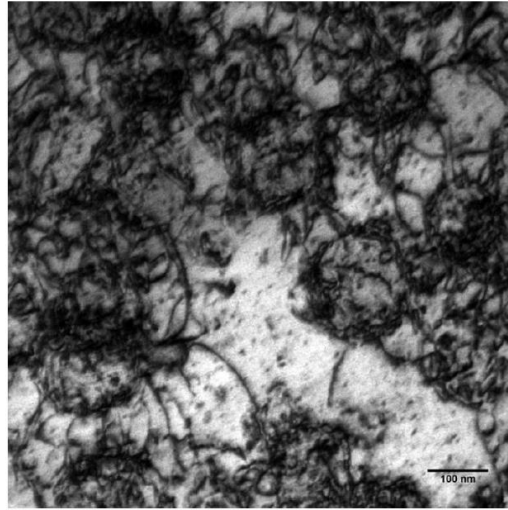


(a)

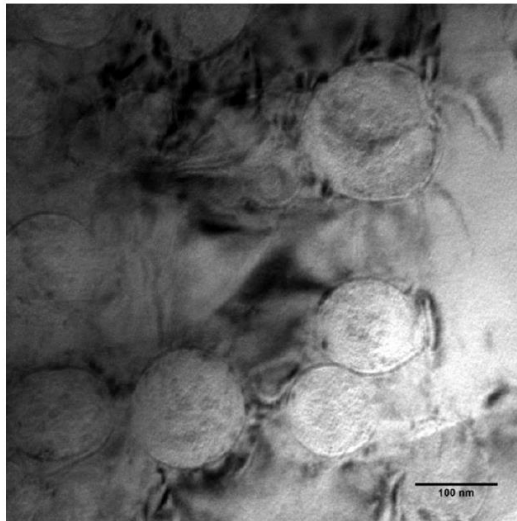


(b)

Figure 3. (a) The evolutions of $\varepsilon_{P,100}$, $\varepsilon_{P,111}$, $\varepsilon_{P,210}$, and ε_M as functions of the initial applied stress and macrostrain at 364 °C. The experimental data are denoted as points, while the FE analysis results are presented as lines.

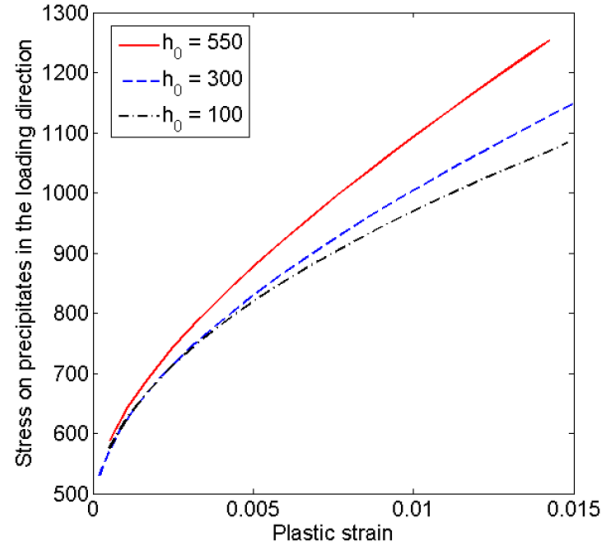


(a)

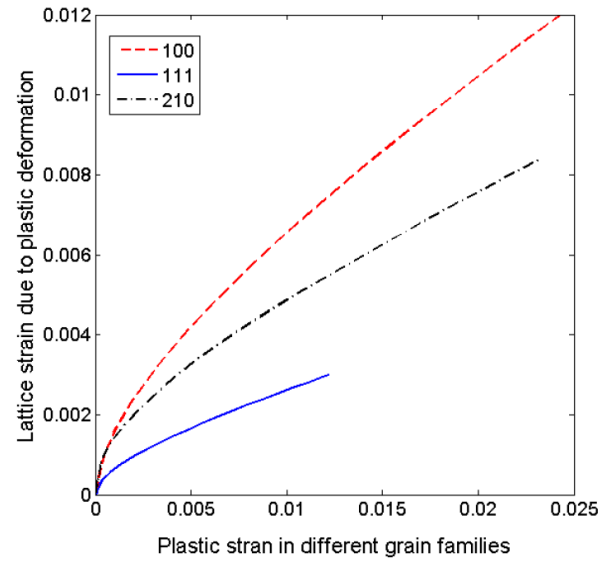


(b)

Figure 5. The microstructure of deformed specimens ($\epsilon \sim 3.5\%$ at $350\text{ }^{\circ}\text{C}$). The image in (b) was taken from the orientation near that in (a).

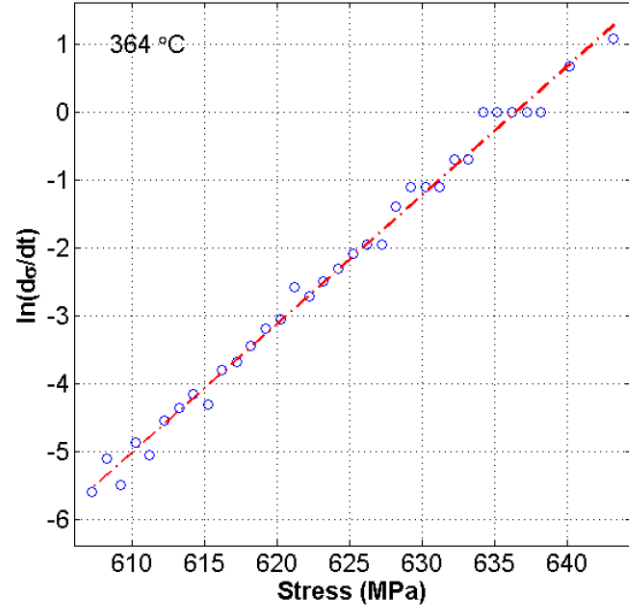


(a)

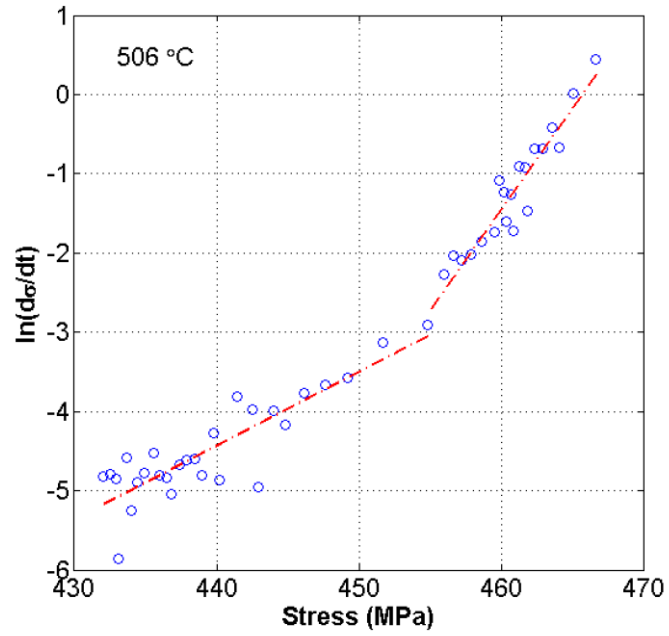


(b)

Figure 6. (a) The stress on precipitates as a function of h_0 ; (b) The anisotropic lattice strain evolution behavior in $\langle 100 \rangle$ -, $\langle 111 \rangle$ -, and $\langle 210 \rangle$ -oriented precipitates. Other parameters (see Supplementary Table S1) keep constant following the FE model at 364 °C in (a).



(c)



(d)

Figure 7. The $\ln(\dot{\sigma})$ vs. σ plots for both tests. The activation volume can be estimated through the slope between $\ln\dot{\sigma}$ and σ (Eq. 2).